

# Advanced novel characterisation of nuclear graphite microstructure via quasi-Bayesian modelling of Scanning Electron Microscopy, N<sub>2</sub> adsorption and Hg porosimetry

Bradley Moresby-White<sup>a</sup>, Katie L. Jones<sup>a,\*</sup>, G. Peter Matthews<sup>a</sup>, Giuliano M. Laudone<sup>a</sup>

<sup>a</sup>*Faculty of Science and Engineering, University of Plymouth, Plymouth, UK*

---

## Abstract

Nuclear grade graphite is a critical component of those Generation IV reactors which are graphite-moderated. Reliable characterisation of its microporous network is crucial for safe and optimal performance. The microstructure, in particular porosity, dictates material properties and the evolution of those properties under operational conditions (i.e., oxidation rates, gas diffusion, and thermal degradation). This project develops and initially validates a methodology for characterising the surface porosity of IG-110 and IG-430 nuclear graphites via computational analysis of composite Scanning Electron Microscopy (SEM) micrographs, covering an FOV (Field of View) comparable with previous Optical Microscopy (OM) -based works (mm<sup>2</sup> scale). Initial integration of surface porosity data into a new version of the PoreXpert void network and pore fluid simulation framework, integrated with Hg porosimetry and N<sub>2</sub> adsorption, produced physically plausible preliminary models of the pore network and simulated pore-fluid flow properties such as tortuosity, diffusivity, and permeability. This enhanced characterisation method forms a further useful methodology in refining models of graphite behaviour, ultimately contributing to the safe and optimal operation of current and proposed graphite-moderated nuclear reactors.

*Keywords:* keyword, keyword, keyword

---

\*Corresponding author.

Email address: [katie.jones@plymouth.ac.uk](mailto:katie.jones@plymouth.ac.uk) (Katie L. Jones)

## 1. Introduction

Graphite, a carbon allotrope, is employed as a moderator, neutron reflector and structural component in Generation IV reactors [1]. Nuclear grade graphite is engineered for this specific use case, characterised by exceptionally low boron content, high structural strength, thermal stability, and a high scattering and low absorbent neutron cross-section [2].

Sufficiently high-volume and fidelity image analysis may enable the constraint of the range of outputs from inverse modelling by adding an extra layer of structural information about a given sample. The dataset resulting from this were used in the validation of PoreXpert™ v.3, where the constraint of the range of possible outputs from inverse modelling via channel porosity is a flagship feature.

The internal microstructure of nuclear grade graphite plays a key role in its mechanical and thermo-physical properties, as well the evolution of these properties under irradiation [1]. Porosity, the proportion of total volume represented by void space, is the defining feature of the microstructure of nuclear-grade graphite. Porosity differs between grades of nuclear grade graphite, as a consequence of varying manufacturing processes and input [3]. Key performance and safety-related phenomena, such as oxidation, gas release and thermal degradation, are modulated by porosity. Oxidation rates are typically higher where open porosity is distributed uniformly, as the ease with which closed pore surface area can be incrementally accessed increases [4]. Porosity also modulates gas diffusion, with a sufficiently strong correlation coefficient to enable the estimation of the effective diffusion coefficient from total porosity alone [5]. Diffusion rate then influences the rate of degradation, determining whether the behaviour under oxidative conditions will be diffusion-controlled or kinetic-controlled [6].

Several experimental techniques exist for the characterisation of porosity, including X-ray Computed Tomography (CT), Mercury (Hg) intrusion porosimetry, Helium (He) pycnometry, and Nitrogen ( $N_2$ ) adsorption [3, 7, 8]. The fundamental physical limitations of the instruments associated with these tech-

niques mean no individual experimental procedure is capable of characterising the full channel or open pore size distribution. These limitations increase the attractiveness of direct characterisation methods, where the pores themselves are imaged, although these methods too have significant limitations.

PoreXpert is a void network simulation package developed at the University of Plymouth. A primary input for its modelling is the percolation characteristic of the sample, usually measured by Hg porosimetry. In the case of nuclear graphite, mercury porosimeters cannot reach sufficient applied pressure to probe the smallest voids of interest, and therefore, the percolation characteristic is extended to smaller void sizes by Grand-Canonical Monte-Carlo interpretation of N<sub>2</sub> adsorption. PoreXpert is a quasi-Bayesian model which proceeds inversely from effect (the percolation) to cause (the void network). PoreXpert constructs an 8 dimensional parameter space, composed of 5 numerical parameters which represent the physical characteristics of the pore network, such as the skew of the void size distribution, and 3 constraining Boolean parameters, for example, to avoid structures where features overlap each other. A Boltzmann-annealed amoeboid simplex searches over this parameter space to find the set of parameters that produces a percolation curve minimally different from the intrusion curve derived from Hg porosimetry and N<sub>2</sub>/Kr adsorption. The final result is a simulated pore network with the correct porosity and percolation properties, on which many simulations, such as pore-fluid permeability and tortuosity, and sample ageing under radiation, can be performed [9].

For the following, perhaps just a summarisation will do as this is expounded upon in modelling section

### *1.1. Literature Review DRAFT PLACEHOLDER TITLE*

The primary objective of this work is to develop and validate a method of quantifying the channel porosity of nuclear-grade graphites via computational image analysis of Scanning Electron Microscopy (SEM) micrographs. The apparent porosity of the surface, which usually includes channels and voids very near the surface, provides an entirely new experimental input for modelling. Since the porosity is derived not only from surface pores but also from pores adjacent to them just below the surface, we refer to the apparent surface porosity

For this I think we need more specificity, and maybe here is the place to talk about sample prep?

as channel porosity rather than surface porosity. The channel porosity estimate replaces or complements porosity estimates from Hg porosimetry and/or pycnometry, which are often difficult to measure or are inaccurate.

Previous investigations have been made into quantifying channel porosity, a form of direct characterisation, either as the primary focus or as part of broader characterisation [10, 11, 12, 13, 14, 15, 3]. Most researchers have employed optical microscopy generating datasets based on thousands of pores, but characterise pore contours rather than pore throats, owing to a low resolution and objective relative to SEM analysis [11, 12, 14]. In addition, the low objective required to image large areas necessitates pore diameter thresholds which reach in some cases  $50 \mu\text{m}^2$ , excluding a significant proportion of the PSD indicated by experimental methods [11, 12, 14].

The fallacy that channel porosity = open porosity is key to cover here too

The SEM-derived channel porosity characterisation of this work utilises composite micrographs, composed of 225 individual micrographs, fused into a single composite micrograph per sample, as with SEM-based characterisation of IG-110 [15]. This affords a comparable area, but resolution and magnification multiple times that of previous OM-based works. The resulting analysis is based on tens of thousands of individual pores forming a channel porosity pore size distribution and percentage, per sample. The comparatively higher resolution of SEM also enables a significantly lower pore diameter threshold, and thus a channel porosity and PSD of significantly improved representativeness.

This method therefore constructs more representative pore network models, leading to network characteristic calculations, such as permeability or diffusivity, which better represent the physical nature of the samples being modelled. The key test of this method is whether modelling a full percolation curve, based on SEM-derived channel porosity, Hg porosimetry, and GCMC modelled N<sub>2</sub> adsorption, generates an open porosity value similar to that measured by pycnometry. If successful, this would indicate that this novel multi-technique method is sound.

## 2. Methodology

### 2.1. Materials

Virgin graphite samples of two grades, IG-110 and IG-430, were supplied by Toyo Tanso Ltd<sup>TM</sup>, Osaka, Japan. The properties of both grades are tabulated (Table 1). IG-110 is employed in the three existing HTGRs worldwide, while IG-430 is designed to deliver increased density, strength, and thermal conductivity for future applications [16].

### 2.2. Sample preparation

Cuboids were subsampled from virgin graphite blocks, with dimensions of approximately 10 mm x 10 mm x 100 mm. The subsamples were further subsampled into cuboids of side lengths 7 mm, providing 3 cuboids per grade. Samples were polished via SiC polishing pads up to a grit size of P5000, to minimise topographical variations induced by sample preparation that may cause artefacts during SEM imaging or low pressure gas adsorption [18, 17]. Samples were sonicated in 2-propanol for 24 h to remove silica particles introduced during polishing, then dried under vacuum for 12 h at  $305 \pm 5^\circ\text{C}$  using the BELPREP-vac (MicrotracBEL, Japan) to remove residual 2-propanol.

### 2.3. Scanning Electron Microscopy (SEM)

The JEOL IT510 Scanning Electron Microscope was employed to generate the contiguous set of micrographs from which the full composite micrograph is assembled. The Image Montage capability within the JEOLInScope package performed this function, capturing multiple micrographs via a motorized stage, moving the electron beam over the specified area with a set overlap for each

Table 1: Formation characteristics and properties of IG-110 and IG-430 nuclear grade graphites [17, 3]

Grade	Coke source	Bulk density/g cm <sup>-3</sup>	Filler particle size/ $\mu\text{m}$	Tensile strength/MPa	Young's modulus/GPa	Thermal conductivity/W m <sup>-1</sup> K <sup>-1</sup>
IG-110	Petrol	1.77	10	25	9.8	120
IG-430	Pitch	1.82	10	37	10.8	140

Table 2: Summary of the contrast and brightness applied by the automatic adjustment of the SEM software package for all micrographs, expressed as percentages of respective maxima for each sample.

Sample	Avg. Contrast (%)	Std. Contrast (%)	Avg. Brightness (%)	Std. Brightness (%)
IG-430B	98.01	1.02	99.69	0.08
IG-430C	98.16	0.82	99.83	0.08
IG-430F	97.70	0.81	99.58	0.14
IG-110B	95.86	0.72	99.26	0.13
IG-110C	94.03	0.93	99.38	0.13
IG-110F	98.20	0.70	99.69	0.13

Table 3: Parameters for composite assembly captured with the JEOL IT510 SEM using Image Montage Mode

Parameters	Value
Magnification ( $\times$ )	1000
Resolution ( $\mu\text{m}/\text{px}$ )	0.1
Surface area per micrograph ( $\mu\text{m}^2$ )	12 288
Overlap (%)	10
Micrographs per sample (n)	225

consecutive micrograph. Applied parameters are tabulated (Table 3). Stigmation, contrast, and brightness were automatically adjusted, with analysis of the metadata for all 1,350 micrographs demonstrating that shifts in contrast and brightness were insignificant, with no impact on the selection of the intensity threshold for the full composite (Table 2).

Each micrograph represents  $12,288 \mu\text{m}^2$  of sample surface, with each sample consisting of 225 micrographs, yielding a total imaging area of  $2.765 \text{ mm}^2$  per sample. With 3 samples analysed per grade, the total scanned area per graphite grade is  $8.294 \text{ mm}^2$ .

#### 2.4. Composite assembly

Stitching/composite assembly, the assembly of the overlapping micrographs into a single composite, was performed via an enhanced phase correlation method,

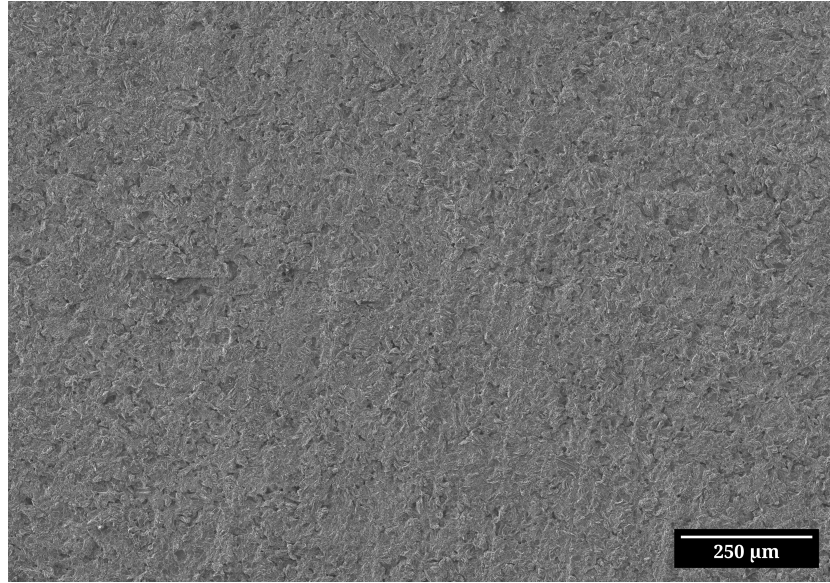


Figure 1: Fully assembled SEM composite: IG-430 Sample C, 1000 $\times$  magnification, 5 kV accelerating voltage. Bar = 250  $\mu\text{m}$ .

operated as an ImageJ plugin [19]. The approach optimises micrograph position globally, is sub-pixel accurate and smooths the transitions between micrographs by a non-linear intensity blending function. Testing indicated that adjustment of the blending parameter had no discernable impact on the final composite micrograph or channel porosity values. Further information can be found in the Supplementary Information.

The resulting composites exhibit no visible delineation between individual micrographs, cover an area comparable with previous works, and distinguish porosity and bulk (Figure 1 [11, 12, 15]).

## 2.5. Computation of Channel Porosity

### 2.5.1. Intensity/Greyscale Thresholding

For the construction of the histogram of intensity, where porosity is to be distinguished, per 8-bit micrograph  $E$  (pixel values  $0 \leq E(x,y) \leq 255$ ), the

intensity histogram  $H(i)$  is computed for  $i = 0, 1, \dots, 255$ .

$$H(i) = \sum_{x=1}^M \sum_{y=1}^N \mathbf{1}\{E(x, y) = i\},$$

where  $M$  and  $N$  are the micrograph width and height (in pixels), and

$$\mathbf{1}\{E(x, y) = i\} = \begin{cases} 1, & \text{if the pixel at } (x, y) \text{ has intensity } i, \\ 0, & \text{otherwise.} \end{cases}$$

The indicator function  $\mathbf{1}\{E(x, y) = i\}$  increments the bin corresponding to that greyscale value. The double sum  $\sum_{x=1}^M \sum_{y=1}^N$  performs across each pixel in the micrograph resulting in a histogram  $H(i)$  of 256 bins, each bin representing number of pixels in the micrograph at each greyscale value  $i$ .

Intensity thresholding, performed on  $H(i)$ , determines a greyscale value at which porosity and bulk (i.e., foreground and background) are distinguished. Global automatic thresholding algorithms optimise by differing criteria (i.e. maximisation of inter-class variance, minimisation of intra-class variance) to determine threshold(s). Thresholding aims to select a greyscale value that binarises porosity, minimising Type I and II errors, as evaluated by the operator.

Evaluation of the 17 automatic global intensity thresholding algorithms available in ImageJ revealed that none were able to distinguish between porosity and bulk with the sensitivity required to allow the classification of pores for the given histogram (Figure 3). In every case, the histogram  $H(i)$  produced by this method exhibited only a single peak, yielding no statistically distinct intensity classes (Figure 2). Automatic thresholding selects a threshold between classes/peaks, consequently, no global intensity thresholding method could distinguish porosity and bulk in this dataset.

A human-in-the-loop (HITL) approach was therefore undertaken (Figure 4). For each sample, the composite was subsampled and examined the threshold determined, then applied to the full composite of that sample. The intensity thresholds were higher in this work than in previous optical microscopy works, at  $0.95 \pm 0.075$  normalized between 0-1 over the 8-bit range of 0-255, capturing the pore throats rather than pore contours. [12, 11].

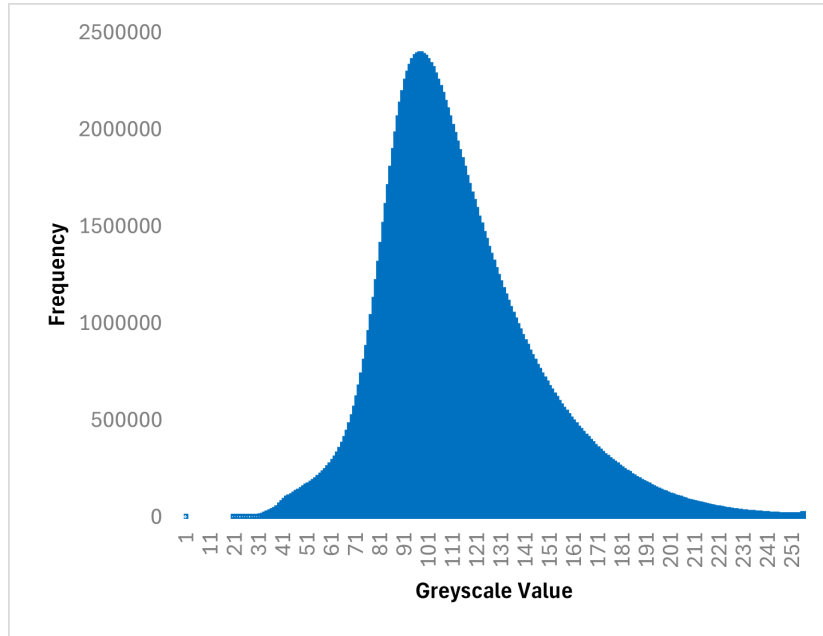


Figure 2: PLACEHOLDER DRAFT: Histogram of greyscale values for IG-430 Sample F, 1000 $\times$ , Showing skewness and unimodality

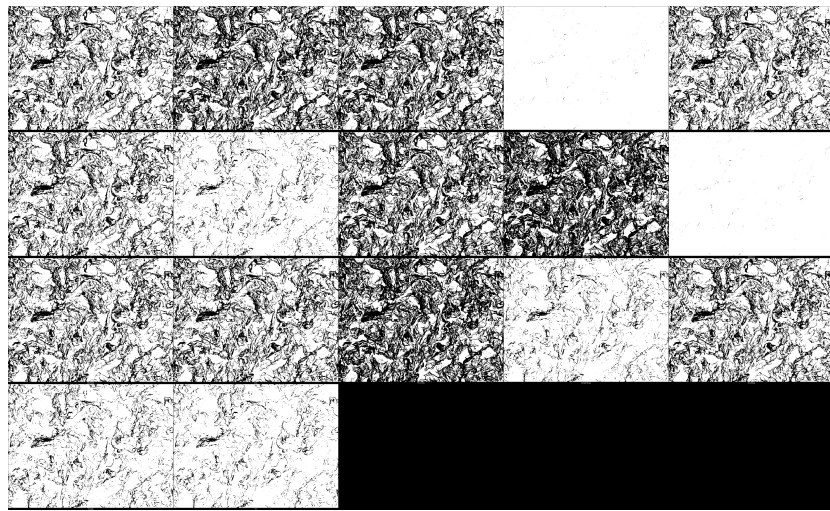


Figure 3: Thresholded Micrograph of IG-430 Sample C at 1000 $\times$  Magnification. Methods are placed sequentially from right to left, row by row. (a) Default (b) Huang (c) Huang2 (d) Intermodes (e) IsoData (f) Li (g) MaxEntropy (h) Mean (i) MinError(I) (j) Minimum (k) Moments (l) Otsu (m) Percentile (n) RenyiEntropy (o) Shanbhag (p) Triangle (q) Yen

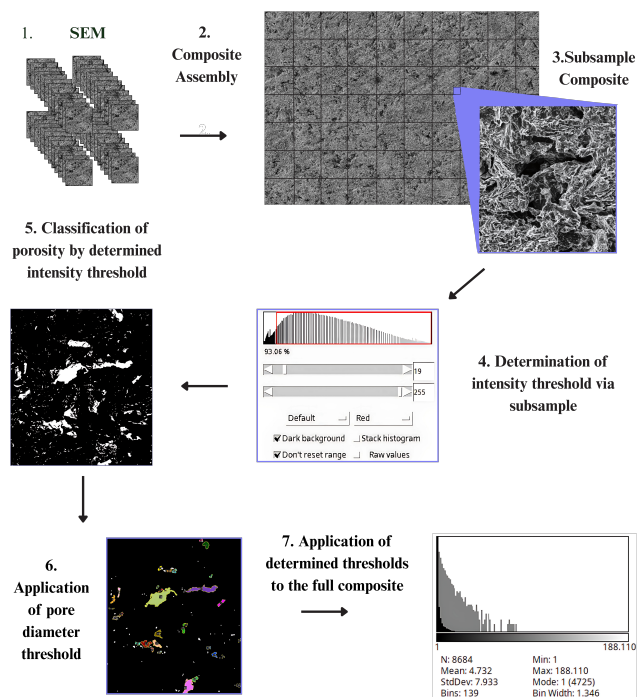


Figure 4: Full thresholding workflow detailing the process of micrograph generation, composite assembly, subsampling, intensity thresholding, and pore diameter thresholding.

Table 4: Effect of different pore area thresholds on a subsection of IG-430F, showing the resulting pore count, total area, average pore size, and percentage area.

Area Threshold ( $\mu\text{m}^2$ )	0	0.5	1	2	4	8
Count	254261	11375	6	4085	2812	1881
Total Area ( $\mu\text{m}^2$ )	71219	56722	53361	50063.63	46518	41161
Average Size ( $\mu\text{m}^2$ )	0.28	4.987	8.229	12.255	16.543	21.883
% Area	4.786	3.812	3.586	3.364	3.126	2.766

An output from this process, selected at random, demonstrates the result of the HITL approach (Figure 5).

### 2.5.2. Pore Diameter Thresholding

Pore size thresholds were imposed in this work to restrict the classification of pores to a range where binarisation is deemed sufficiently accurate via sensitivity analysis [14, 11, 12].

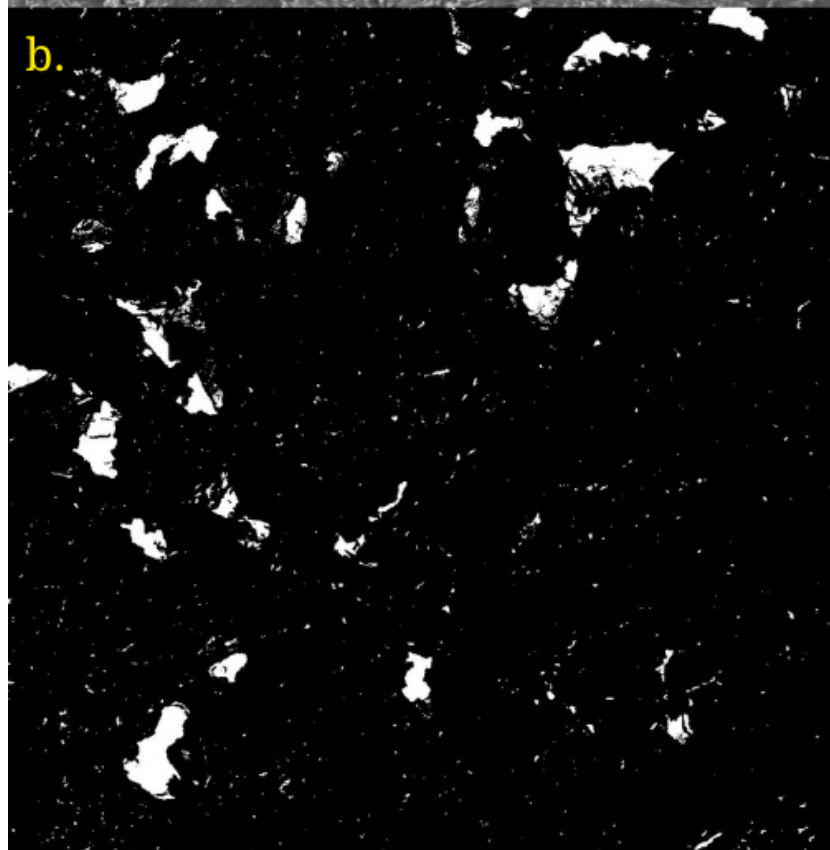
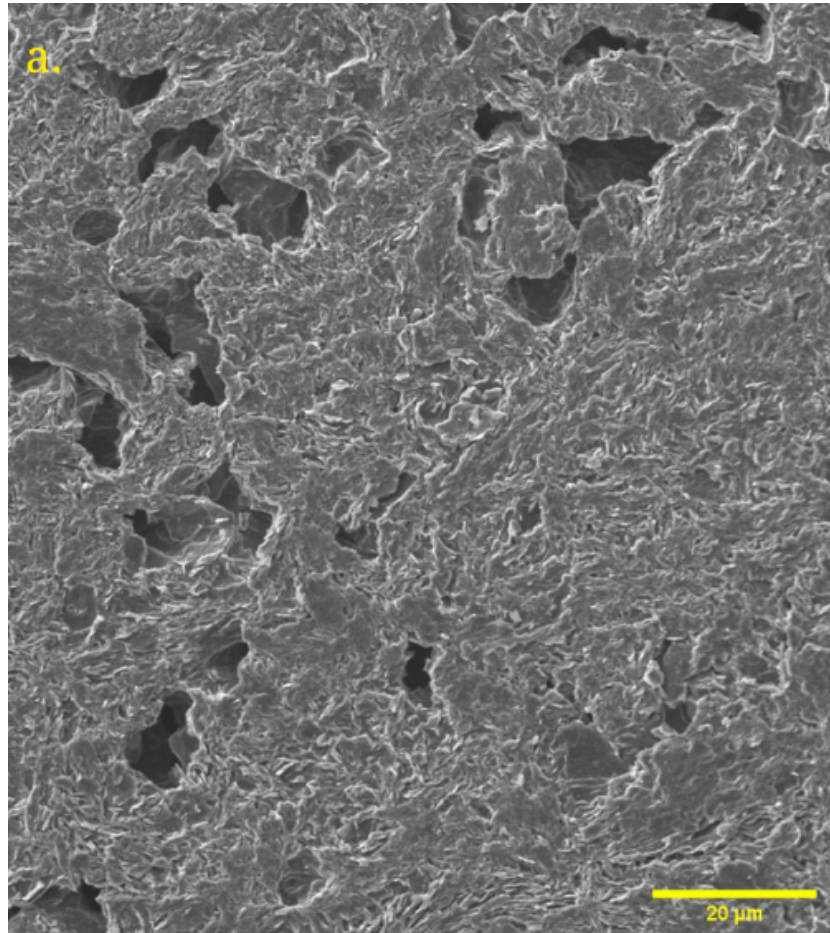
Significant changes in the total pore count result from minor alterations to the threshold (Table 4). The total area of pores exhibits significantly less variation as a function of pore diameter threshold (Table 4). Analysis of the resulting PSDs and sensitivity analysis at each threshold as indicated a pore area threshold of  $1 \mu\text{m}^2$  (diameter =  $1.12 \mu\text{m}$ ) was the optimal compromise between Type I and II errors (Figure 6, Table 4),

### 2.5.3. Channel Porosity Analysis and Calculation

Channel porosity was calculated using the “Analyse Particles” function in ImageJ, identifying pixels surpassing the intensity threshold, generating connected regions (i.e., pores) via a flood-fill algorithm. Connectivity in the flood fill algorithm was based on the 8-connected (Moore neighbourhood) criterion, where a pixel at  $(x, y)$  is considered connected to its eight immediate neighbours:

$$(x - 1, y - 1), (x - 1, y), (x - 1, y + 1), (x, y - 1),$$

$$(x, y + 1), (x + 1, y - 1), (x + 1, y), (x + 1, y + 1)$$



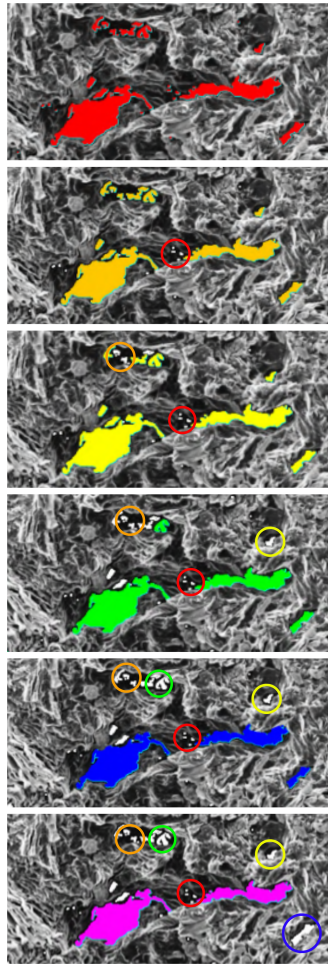


Figure 6: Effect of minimum area threshold on pore identification in subsample of IG-110 Sample B. Highlighted circles denote features which surpassed the previous threshold(s) only, indicated by colour. Thresholds applied (a-f, left-to-right, top-to-bottom): None,  $0.5 \mu\text{m}^2$ ,  $1 \mu\text{m}^2$ ,  $2 \mu\text{m}^2$ ,  $4 \mu\text{m}^2$ , and  $8 \mu\text{m}^2$ .

Any two pixels that exceed the intensity threshold and are either directly adjacent or diagonally connected are classified as belonging to the same region (pore). The area and diameter per pore is calculated by converting the pixel count into physical area (i.e., 10 pixels per micrometre). Regions that do not meet the area/diameter threshold are omitted.

Output from intensity thresholding and pore diameter thresholding for the above parameters is exemplified (Figure 7). The final output was both a pore size distribution (PSD) and channel porosity (%) per sample.

### *2.6. Helium (He) Pycnometry*

Helium pycnometry measures the volume of solids via gas displacement, applying Boyle's Law for multiple states from which density can be derived for a known mass 1.

$$P_1 V_1 = P_2 V_2 \quad (1)$$

The dataset containing Skeletal density measurements, and calculations of Closed Pore Volume (CPV), Open Pore Volume (OPV), and Specific Pore Volume (SPV) generated by Jones et al. was used [17]. This dataset represents helium pycnometry measurements performed on IG-110 and IG-430 sampled from the same block as those samples which underwent SEM imaging in this work.

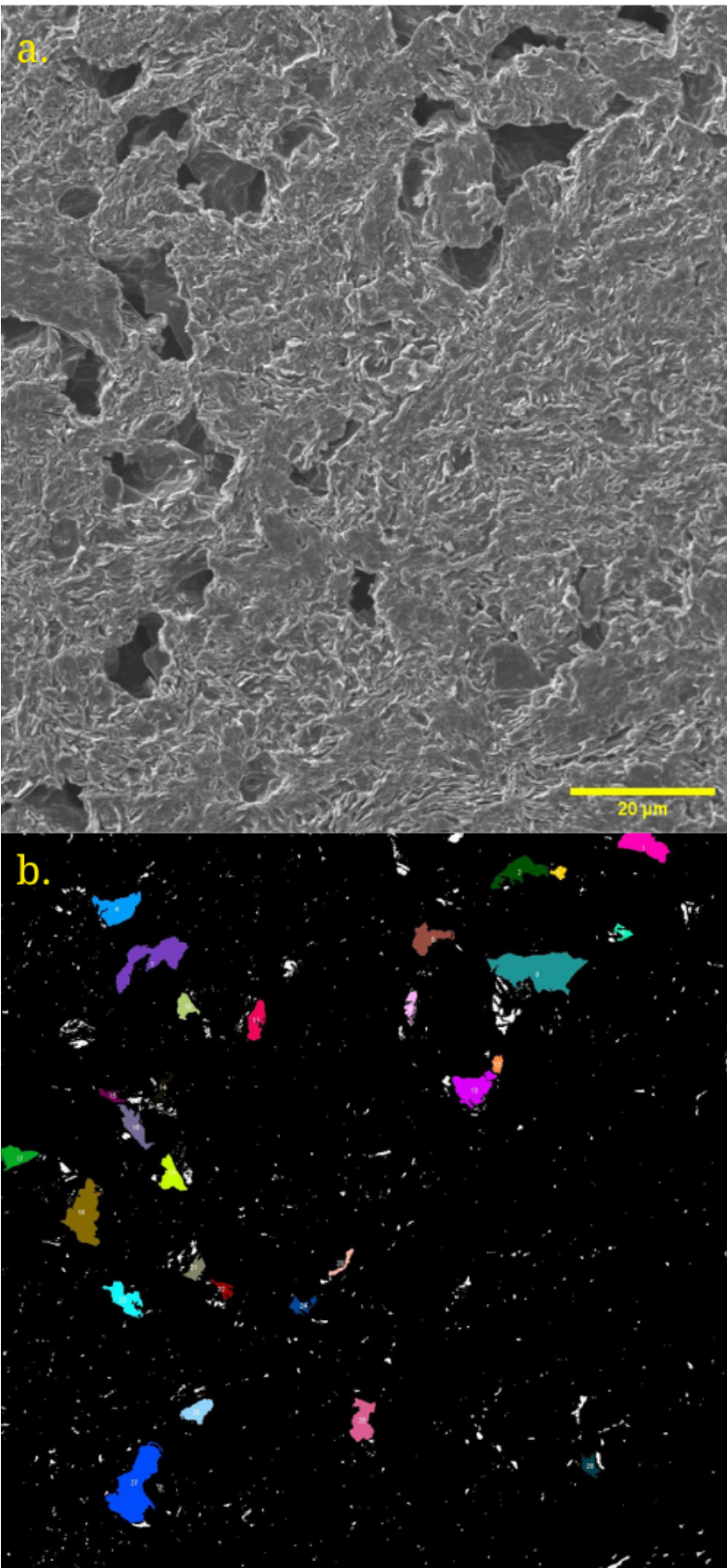
A Pycnomatic ATC pycnometer (Thermo Fisher Scientific, Italy) was used to generate this dataset. Measurements were performed at a temperature of  $20.00 \pm 0.01^\circ\text{C}$ , for ten replicates per sample, calculating the arithmetic mean.

Solid phase volume  $V_{\text{SOLID}}$  was calculated assuming a theoretical density of  $2.26 \text{ g cm}^{-3}$  for an idealised graphite crystal.

### *2.7. Mercury (Hg) Intrusion Porosimetry*

Mercury intrusion porosimetry operates on the principle that the pressure at which a non-wetting fluid intrudes a pore is inversely proportional to the diameter of that pore.

I mean really it is about connectivity right? But anyhow I might just leave it as is.



The exact physical relationship between diameter and applied pressure is governed by the Laplace Equation (Eq. 2)

$$d = \frac{-4\gamma \cos \theta}{P} \quad (2)$$

- $d$  (m): Pore diameter
- $\gamma$  (N/m): Surface tension of the fluid
- $\theta$  (degrees): Contact angle of the fluid with the surface
- $P$  (Pa): Pressure

$140^\circ$  and  $130^\circ$  were the values assumed for advancing and receding contact angles respectively.  $0.480 \text{ N m}^{-1}$  was taken for the surface tension of mercury [20].

In this work, the dataset generated by Jones et al. [17] was used, representing mercury intrusion porosimetry performed on IG-110 and IG-430 sampled from the same block as those samples which underwent SEM imaging in this work.

### 2.8. Nitrogen ( $N_2$ ) Adsorption

Low-pressure gas adsorption isotherms were obtained using a BELSORP-max (MicrotracBEL, Japan) volumetric gas adsorption instrument.

The dataset generated by Jones *et al.* [17] was used in this work, representing nitrogen adsorption measurements performed on IG-110 and IG-430 sampled from the same block as those samples which underwent SEM imaging in this work.

## 3. Modelling

PoreXpert is a quasi-Bayesian modelling software which proceeds inversely from effect (the percolation) to cause (the void network). The software constructs an 8-dimensional parameter space, composed of 5 numerical parameters

which represent the physical characteristics of the pore network, and 3 constraining Boolean parameters. A Boltzmann-annealed amoeboid simplex searches over this parameter space to find the set of parameters that produces a percolation curve minimally different from the intrusion curve derived from Hg porosimetry and N<sub>2</sub>/Kr adsorption. The intrusion curve is formed of experimental output from both methods as mercury porosimetry cannot reach sufficient pressure to probe the smallest voids of interest, and therefore, the percolation characteristic is extended to smaller void sizes by Grand-Canonical Monte-Carlo interpretation of N<sub>2</sub> adsorption. The output is a simulated pore network with the matching porosity and percolation properties, on which simulations such as pore-fluid permeability and tortuosity can be performed (Figure 10 [9]).

During modelling, the approximation type reflecting the depth of SEM analysis into the porous structure is selected by the user (Figure ??, [9]). Approximation Type 2 *Surface connected throats and the visible volumes of connected pores* was determined to be the optimal approximation for the channel porosity dataset, following examination of the micrographs.

Channel porosity (%), minimum, and maximum pore diameter were input into the modelling software. The implementation of a minimum and maximum pore diameter enables the model to adjust the extent of the PSD which the channel porosity estimates. For the initial test sample IG-110B, the simulated intrusion curve was optimised to a 1.91% deviation from the experimental curve.

(Figure 9)

Initial modelling outputs were congruent with manufacturer data as exemplified for IG-110 Sample B, with an estimated open porosity of 20%, as compared to the 19.62% figure for the open porosity of IG-110, for Toyo Tanso Ltd™(Table 1).

The weak correlation ( $r^2 = 0.32$ ) between open porosity estimate and distance between simulated and experimental percolation characteristic indicates that averaging over all stochastic generations is a valid measure of this method's estimate of open porosity.

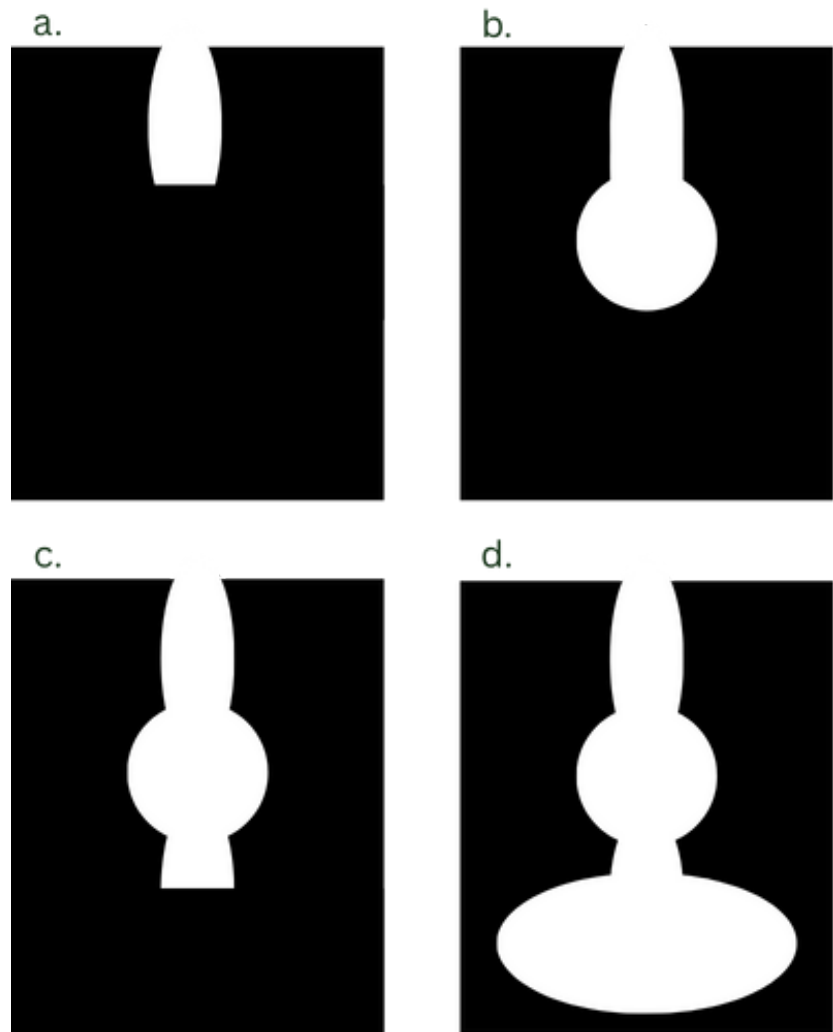


Figure 8: Representation of approximation types 1–4. White regions indicate porosity visible to the SEM, while black represents bulk. (a) Surface-connected throats only. (b) Surface-connected throats along with the visible volumes of connected pores. (c) Surface-connected throats, visible volumes of connected pores, and any throats located beneath them. (d) All vertically aligned features in the top layer, including both surface-connected and unconnected elements.

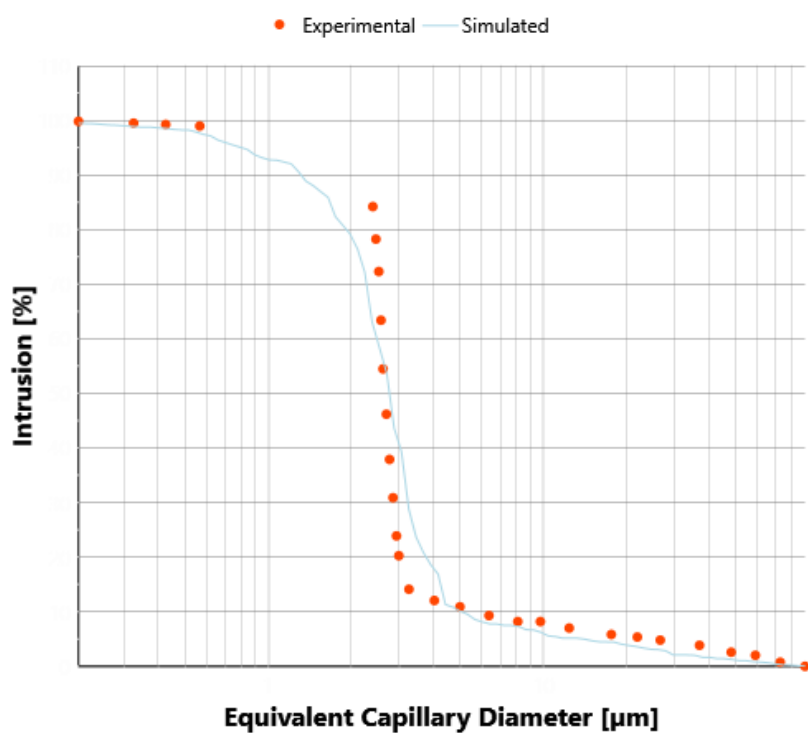


Figure 9: Comparison of the simulated intrusion curve with the experimental data. Orange dots represent experimental data points, while the blue line corresponds to the simulated percolation curve generated from the pore network model.

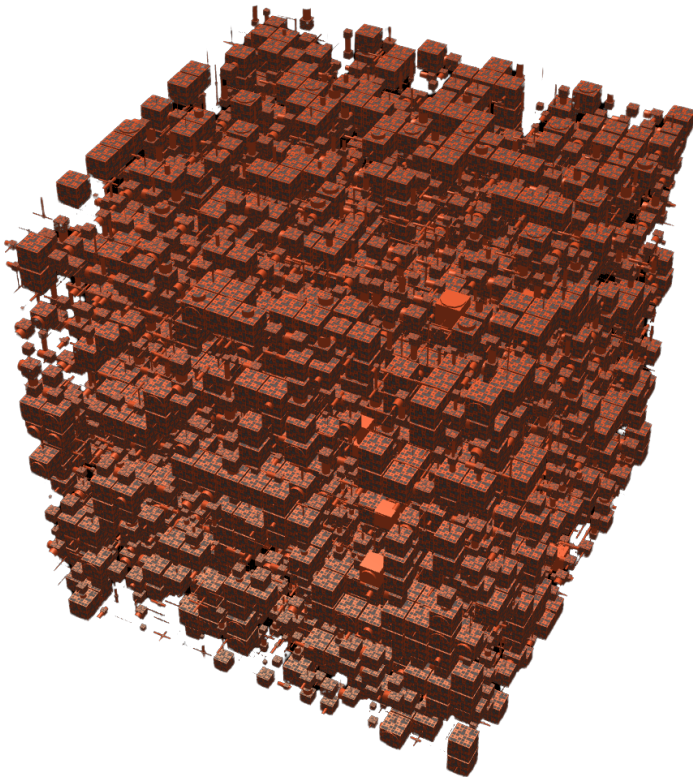


Figure 10: Pore network resulting from the integration of channel porosity and experimental data by the workflows above. 1.91% distance between simulated and experimental curves, following the application of Approximation Type 2 (Figure 8). Channel Porosity estimation was averaged over the top 9 layers of a unit cell 20x20x20. The result of one generation of stochastic number generation.

Table 5: Pore Size Distribution (PSD) and summary characteristics for IG-110 and IG-430 samples.

Sample	n / pores	Total Area / $\mu\text{m}^2$	Channel Porosity / %
IG-110 B	8,684	41,091	3.14
IG-110 C	7,075	49,755	3.27
IG-110 F	8,296	50,735	3.38
IG-430 B	6,848	32,983	2.30
IG-430 C	13,026	49,534	2.94
IG-430 F	6,819	56,794	3.66

#### 4. Results

The completed workflow of SEM imaging and computational composite analysis yielded estimates of channel porosity for both graphite grades (Table 5). IG-110 samples exhibited channel porosity values ranging from 3.14-3.38%, while channel porosity for IG-430 samples ranged from 2.30-3.66%

Area contribution distribution is represented graphically for both graphite grades (Figure 11, 12). The area of each logarithmic bin (spanning 0.1-100  $\mu\text{m}$  on the x-axis) was summed then divided by the bin width in  $\log_{10}(D)$  to derive  $dS/d(\log_{10} D)$ , with the x-axis then linearised and constrained. y-axis values represent area density in  $\mu\text{m}^2$  per  $\log_{10}(D)$ .

IG-110 and IG-430 exhibit peaks between at 3-7  $\mu\text{m}$ . [15] found that channel porosity as classified by SEM was 3% for IG-110, which is highly congruent with the 3.14-3.38% range derived in this work.

Interpolation via the adjustment of the intensity threshold to match previous OM works (i.e., pore contours are classified, as opposed to pore throats) produces results consistent with previous works. [12] derive a channel porosity of 14.73% for IG-110, with [11] deriving 14% for the same grade, congruent with the 13-14% channel porosity derived by this work following interpolation.

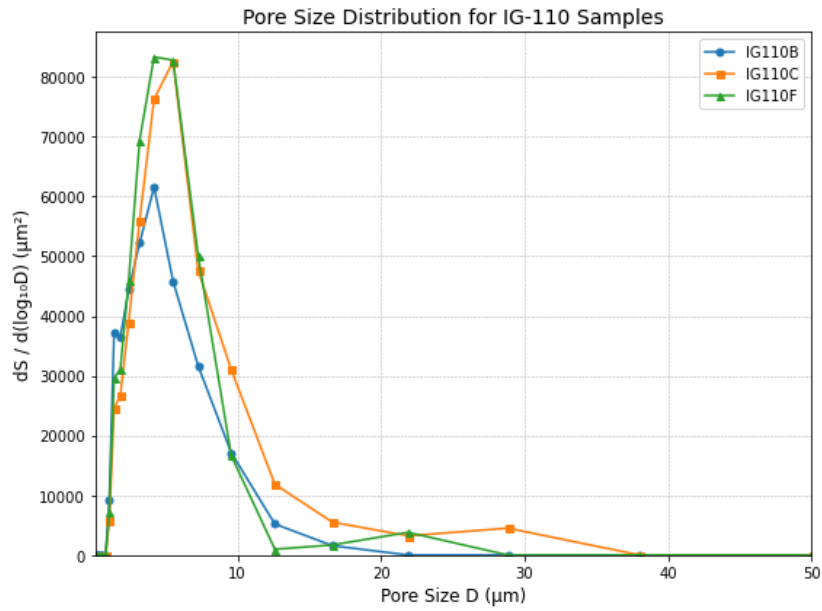


Figure 11: DRAFT: I want to recheck my code on these distributions

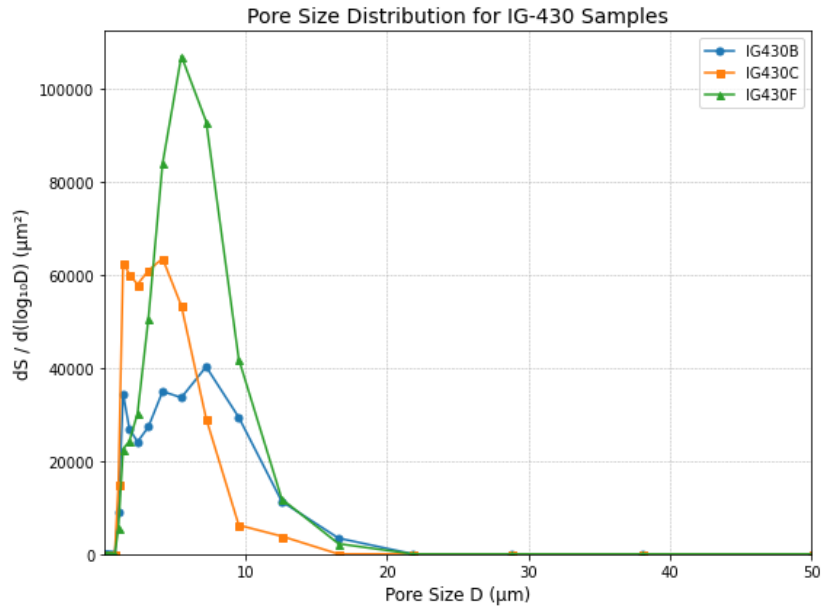


Figure 12: DRAFT: I want to recheck my code on these distributions

## 5. Discussion

### 5.1. Channel Porosity Overestimation due to connectivity algo

This algorithm is likely to yield at least a slight overestimation of the average pore size. This is because such an inclusive definition means that two or more pores, connected by a narrow neck or even simply with adjacent pixels, would be classified as a single pore. Notably, this would not change the final channel porosity (%), nor the modelling, as it utilises only the channel porosity %. However, this would result in a rightward shift in the PSD. Skeleton segmentation is for fine-grade nuclear graphite likely to be a more accurate approach than a simple connectivity algorithm as used here would be a key improvement if implemented [3]

### 5.2. Pore Diameter Threshold Discussion

Setting the pore diameter threshold does not imply that no pores exist below this limit. Rather, it acknowledges that the confidence in classifying pores below the threshold is too low for reliable use. In this work, the limitations of any single technique are compensated by the strengths of others. during modelling, an interval is selected over which the channel porosity determined from SEM imaging can reliably constrain the outputs of the inverse modelling process. Thus, no type II errors are introduced in the final model due to pore size thresholding, thanks to the combined use of alternative techniques and the ability to specify an interval within PoreXpert v.3.

### 5.3. Pore Fragmentation and Implications for Modelling

The application of a maximum pore diameter is a key part of the modelling as initial modelling where this was not implemented failed to yield reliable results. It is believed that this is due to the impossibility of the model fitting an plausible network on the premise that pores from 1.12  $\mu\text{m}$  diameter upwards represent only 3 % of the sample surface. Imposing an upper threshold as the simple max of the pore diameters identified by SEM is an uncomplicated initial solution

This part really requires Peter's insight as to the actual functioning of the program

This is not the key issue. The real thing is the accuracy of the pore size distribution generated by SEM.

For example, the modelling would I think be distorted completely by saying that 3% of the sample surface is made up of pores of 1.12-25  $\mu\text{m}$  diameter.

which has more logical implications (i.e., to state that between 1.12 and 20 $\mu$ m diameter, 3% of the sample surface is represented by porosity). This threshold varied between 13-26  $\mu$ m in this work, which should cover the vast majority of the porosity, particularly given the pore fragmentation issue described below.

Specifically, the use of a simple Moore neighbourhood connectivity, when combined with the fact that Erosion and Dilation binary operations were not applied, means that pores which the operator identifies as a single pore are in more than one case instead defined as two or more pores. Not only this but these split pores may not then surpass the pore diameter threshold of 1.12 $\mu$ m. (e.g., a pore of 10 $\mu$ m diameter might be split into 2 pores, 1 of 9 $\mu$ m diameter and another of 1 $\mu$ m diameter, which would be discarded due to the pore diameter threshold, reducing the channel porosity % and shifting rightward the pore size distribution).

The end result is that it is difficult to describe the pore size distribution derived from SEM as it currently stands, as completely impenetrable. Crucially, the production of reasonable results from the modelling as above depends on an accurate constraint of the pore diameter interval (i.e., the channel porosity figure of 3% refers only to porosity between 1.12 and 25 $\mu$ m diameter) and so not only the SEM-derived pore size distribution but the PX modelling which uses it, has at least some reduction in reliability due to the pore fragmentation issue. However, this is likely a soluble problem, as follows (look at workflow).

#### *5.4. Proposed Future Workflow*

-Just my idea of an improved workflow: 1. Resin Impregnation 2. SEM (see if we can go to 2kV) 3. Otsu Thresholding (We have clear bimodality thanks to Resin impregnation) 4. Skeleton segmentation (Avizo software needed?) 5. Apply improved pore diameter thresholds, or maybe do not do any at all as no longer needed? At least lowered. 6. Modelling

#### *5.5. Proposed Improved Sample Preparation*

Could talk here about how we wanted to do resin impeg like Kane et al, but did not have the chance, and explain this might introduce issues, also we could talk about how this is quite rough, and that this

## 6. Supplementary Information

One advantage of this method is the avoidance of error propagation by consecutive registration steps, as simply placing micrograph A relative to micrograph B, and then micrograph B relative to micrograph C, would result in accumulation of errors. This method builds a graph whose nodes are the micrographs, and edges are the measured pairwise shifts between the micrographs. It then finds the set of micrograph positions that minimise the total squared registration error across the entire graph, a form of globally optimised registration [19].

This stitching method also allows sub-pixel accuracy, which is crucial for accurate pore measurement. For any two micrographs  $A$  and  $B$ , which are shifted relative to each other (i.e., micrograph  $B$  is shifted two pixels up and 10 pixels left of micrograph  $A$ ) then their Fourier transforms would have the same magnitude but different phases. A normalized cross-power spectrum isolates the phase difference, and the Inverse Fourier transform yields a correlation map with peaks indicating possible translations between the micrographs. The complexity of real images and the periodicity of the Fourier transform means that the correlation map is not a single peak, but rather a set of peaks, each representing a possible translation. This method therefore selects the  $n$  highest local maxima and finds the peak with the best correlation, which it defines as the true translation between the two micrographs [19]. Finally, sub-pixel accuracy in that shift is achieved by applying a parabolic interpolation around the selected peak to refine the translation estimate.

Additionally, a non-linear intensity blending function eliminates the visible seams between micrographs, which can occur even when the micrographs are perfectly aligned due to shading variations. This blending assigns a weight to each pixel in a tile, working as a function of the distance from the tile edge, with a tunable parameter controlling this weighting function. In non-overlapping regions, the centre of the micrograph, the weight is essentially 1, so the original pixel value is preserved exactly. In overlapping regions, intensities are a convex

combination of the original values. Crucially, because the weights sum to 1 everywhere, blended intensity is simply a weighted average of the original intensities. Thus, the final composite micrograph is still a valid representation of the original micrographs, but the seams have been removed. [19] The removal of the visible seams between micrographs did increase confidence that in the following steps, the subsample used to determine the intensity threshold was representative of the full composite micrograph.

## References

- [1] B. Marsden, A. Jones, G. Hall, M. Treifi, P. Mummery, 14 - graphite as a core material for generation iv nuclear reactors, in: P. Yvon (Ed.), Structural Materials for Generation IV Nuclear Reactors, Woodhead Publishing, 2017, pp. 495–532. doi:<https://doi.org/10.1016/B978-0-08-100906-2.00014-8>  
URL <https://www.sciencedirect.com/science/article/pii/B9780081009062000148>
- [2] B. J. Marsden, M. Haverty, W. Bodel, G. N. Hall, A. N. Jones, P. M. Mummery, M. Treifi, Dimensional change, irradiation creep and thermal/mechanical property changes in nuclear graphite, International Materials Reviews 61 (3) (2016) 155–182. doi:10.1080/09506608.2015.1136460.  
URL <https://doi.org/10.1080/09506608.2015.1136460>
- [3] J. D. Arregui-Mena, R. N. Worth, W. Bodel, B. März, W. Li, A. A. Campbell, E. Cakmak, N. Gallego, C. Contescu, P. D. Edmondson, Multiscale characterization and comparison of historical and modern nuclear graphite grades, Materials Characterization 190 (2022) 112047. doi:<https://doi.org/10.1016/j.matchar.2022.112047>.  
URL <https://www.sciencedirect.com/science/article/pii/S1044580322003291>
- [4] R. M. Paul, J. D. Arregui-Mena, C. I. Contescu, N. C. Gallego, Effect of microstructure and temperature on nuclear graphite oxidation using the 3d random pore model, Carbon 191 (2022) 132–145. doi:<https://doi.org/10.1016/j.carbon.2022.01.041>.  
URL <https://www.sciencedirect.com/science/article/pii/S0008622322000501>
- [5] J. J. Kane, A. C. Matthews, C. J. Orme, C. I. Contescu, W. D. Swank, W. E. Windes, Effective gaseous diffusion coefficients of select ultra-fine, super-fine and medium grain nuclear graphite, Carbon 136 (2018) 369–379. doi:<https://doi.org/10.1016/j.carbon.2018.05.003>.  
URL <https://www.sciencedirect.com/science/article/pii/S0008622318304548>

- [6] A. C. Matthews, J. J. Kane, W. D. Swank, W. E. Windes, Nuclear graphite strength degradation under varying oxidizing conditions, Nuclear Engineering and Design 379 (2021) 111245. doi:<https://doi.org/10.1016/j.nucengdes.2021.111245>. URL <https://www.sciencedirect.com/science/article/pii/S0029549321001977>
- [7] K. L. Jones, G. P. Matthews, G. M. Laudone, The effect of irradiation and radiolytic oxidation on the porous space of gilsocarbon nuclear graphite measured with mercury porosimetry and helium pycnometry, Carbon 158 (2020) 256–266. doi:<https://doi.org/10.1016/j.carbon.2019.11.084>. URL <https://www.sciencedirect.com/science/article/pii/S0008622319312175>
- [8] C. I. Contescu, J. D. Arregui-Mena, A. A. Campbell, P. D. Edmondson, N. C. Gallego, K. Takizawa, Y. Katoh, Development of mesopores in superfine grain graphite neutron-irradiated at high fluence, Carbon 141 (2019) 663–675. doi:<https://doi.org/10.1016/j.carbon.2018.08.039>. URL <https://www.sciencedirect.com/science/article/pii/S0008622318307723>
- [9] G. P. Matthews, PoreXpert User Manual: A comprehensive guide to version 3, PoreXpert Ltd, Plymouth, UK, 3rd Edition, director and CEO, PoreXpert Ltd; Emeritus Professor of Applied Physical Chemistry, University of Plymouth, UK. Includes introductory tutorials, fundamental science sections, guidance on avoiding common experimental errors, and software validation. (2025). URL <https://www.porexpert.com/>
- [10] W.-H. Huang, et al., The relationship between microstructure and oxidation effects of selected ig- and nbg-grade nuclear graphites, Journal of Nuclear Materials 454 (1) (2014) 149–158. doi:[10.1016/j.jnucmat.2014.07.052](https://doi.org/10.1016/j.jnucmat.2014.07.052).
- [11] Q. Huang, H. Tang, Porosity analysis of superfine-grain graphite ig-110 and ultrafine-grain graphite t220, Materials Science and Technology 35 (8) (2019) 962–968. doi:[10.1080/02670836.2019.1599557](https://doi.org/10.1080/02670836.2019.1599557).

- [12] J. Kane, et al., Microstructural characterization and pore structure analysis of nuclear graphite, *Journal of Nuclear Materials* 415 (2) (2011) 189–197. doi:10.1016/j.jnucmat.2011.05.053.
- [13] E. Kim, J. Song, S. Hong, Characterization of pore structure of nuclear grade graphite using image analysis technique and mercury porosimetry, <https://www.osti.gov/etdeweb/biblio/21493402>, accessed: 10 January 2025 (2010).
- [14] J. Taylor, G. Hall, P. Mummery, Investigating the effects of stress on the pore structures of nuclear grade graphites, *Journal of Nuclear Materials* 470 (2016) 216–228. doi:10.1016/j.jnucmat.2015.12.031.
- [15] Q. Huang, H. Tang, A statistical analysis of pores and microcracks in nuclear graphite, Shanghai Institute of Applied Physics, Chinese Academy of SciencesCorrespondence to Qing Huang, Email: huangqing2012@sinap.ac.cn (2021).
- [16] Toyo Tanso Co., Ltd., Atomic power and nuclear fusion, accessed April 21, 2025 (2025).  
URL <https://www.toyotanso.com/us/en/Products/application/atomic-nuclear.html>
- [17] K. Jones, G. Laudone, G. Matthews, A multi-technique experimental and modelling study of the porous structure of ig-110 and ig-430 nuclear graphite, *Carbon* 128 (2018) 1–11. doi:10.1016/j.carbon.2017.11.076.
- [18] N. Fang, R. Birch, T. Britton, Optimizing broad ion beam polishing of zircaloy-4 for electron backscatter diffraction analysis, *Micron* 159 (2022) 103268. doi:10.1016/j.micron.2022.103268.
- [19] S. Preibisch, S. Saalfeld, P. Tomancak, Globally optimal stitching of tiled 3d microscopic image acquisitions, *Bioinformatics* 25 (11) (2009) 1463–1465. arXiv:2009 Apr 3, doi:10.1093/bioinformatics/btp184.
- [20] J. Van Brakel, S. Modrý, M. Svatá, Mercury porosimetry: state of the art, *Powder Technology* 29 (1) (1981) 1–12. doi:<https://doi.org/10.1016/0032->

5910(81)85001-2.

URL <https://www.sciencedirect.com/science/article/pii/0032591081850012>